Solar Survey: Development and Validation of a Smartphone-Based Solar Site Assessment Tool

Joseph A. Ranalli
Penn State Hazleton
jar339@psu.edu

Abstract

Solar site surveys are an important step in assessing the suitability of a site for a proposed solar power installation. This paper details investigation into the suitability of the Android smartphone platform to serve as a base for site survey applications. Lessons learned are shared based upon development and validation of a prototype application. The prototype application is Solar Survey, a free, open-source application for Android-based smartphones that allows site surveys to be performed. The app uses sensors built into the smartphone to make measurements of the horizon. The measurements may be output in a format suitable for use by System Advisor Model, or other computer tools, to perform more detailed photovoltaic system modelling and economic calculations. In addition, the measurements can be used within the app itself to provide estimates of the available irradiance using the Perez, or other tilted irradiance model. Optimum orientation (relative to irradiance) can be computed for both the raw meteorological data and including the effect of shading. The irradiance and shading calculations were validated against results produced by System Advisor Model. Horizon measurement uncertainty was estimated using repeated measurements of a fixed horizon. It is hoped that through the open-source code and documentation of the methodology in public literature, Solar Survey may serve as a research platform for solar site assessment, and promote further analysis of the accuracy of similar tools.

1. Introduction

An important step in the design and evaluation of a solar installation is an analysis of the proposed site (Galli and Hoberg, 2009). Site analysis provides estimates of the energy production of a hypothetical installation. These estimates allow a variety of detailed design calculations to be performed. Some example applications are: comparisons between several proposed sites, comparisons of various solar technology options for the installation, and assessment of shading and optimum collector orientation (Lave and Kleissl, 2011). Additionally, estimates of a site's energy production form an important piece of an economic analysis for an installation. Besides guiding interpretation of the lifecycle value of a solar installation, these economic analyses play a key role in securing loans or other forms of financial support. Improving the confidence that can be placed on a solar site analysis may help to improve the "bankability" of a proposal (Vignola et al., 2012) and may reduce the cost of money for a project.

Part of a complete site analysis consists of assessing the impact of shading on the solar resource. Shading occurs when obstacles in the surrounding environment obstruct the sunlight from reaching the collector. This can impact both the beam and diffuse components of the resource. Shading impacts all types of solar energy collection systems, but is of particular importance to photovoltaic systems. The electrical properties of a photovoltaic system result in non-linear dependency of system output on shading; small patches of shading on a module can result in disproportionate reductions in the module

power. Models exist by which the electrical mismatch caused by shading can be applied on a cell-by-cell basis to predict the overall behavior of a shaded module (Bishop, 1988). Techniques have also been proposed to compute the cell-by-cell shading based on knowledge of the shading geometry (Goss et al., 2014).

While cell-by-cell modeling techniques are available, this level of detail is not typically found in the shading measurement tools that are available in the marketplace. This may be due in part to the additional complexity involved in obtaining the actual obstacle geometry required to develop a full 3D model of the shading on a solar array. Several methods exist for performing a more general shading analysis. These involve the measurement of the horizon from the perspective of the solar collector, and assume a result based on a small number of point measurements. Such methods span a broad gamut of complexity. The simplest methods employ a theodolite for manually measuring the azimuth and elevation of obstacles and result in a plot of the measured angles on a sun chart. More advanced techniques include commercial tools, such as SolarPathfinder (Solar Pathfinder, 2008) or Solmetric SunEye (Solmetric Corporation, 2011), that acquire measurements of the horizon based on digital image processing of photographs. Of these digital platform tools that are available, many provide preliminary resource analysis in addition to measurement of the horizon.

A review of several commercial shading measurement tools was conducted by Duluk *et al*. (Duluk et al., 2013). In comparing the features and performance of the available tools, Duluk *et al*. identify several shortcomings and areas for improvement. None of the tools they identified provides differentiation between diffuse, beam and ground reflected components of the irradiance. Additionally, they note that comparisons between tools produce different results. In particular, this final shortcoming represents an issue with regard to user confidence in tool validity and the ability of users to scientifically evaluate the analysis performed by the tool.

The purpose of this study is to investigate the suitability the Android smartphone platform for implementation of existing solar resource analysis methodologies toward creating a site analysis and research tool. According to the Pew Research Center, 64% of American adults owned a smartphone in 2015 (Smith, 2015), making it a convenient platform for many potential solar consumers. Additionally, smartphones are built with many of the capabilities needed in order to perform a site survey, reducing the need for additional, potentially expensive hardware. While implementations of the site survey vary among the existing tools available, the general capabilities required are:

- the ability to identify the geographic location in which the measurement is made
- the ability to visualize the horizon in some way (requiring knowledge of azimuth/altitude positions of obstacles relative to the measurement)
- the ability to perform computations related to determining solar positioning, in order to determine hour-by-hour shading for the measurement location
- the ability to produce horizon measurement data that is readily used by other computer-based site analysis tools

This study aims to evaluate the suitability of the Android platform relative to these capabilities for site survey applications, and to create a prototype platform for site survey testing that offers lessons learned related to use of Android as a platform for this purpose. The prototype tool developed in this study, Solar Survey, is a free, open source application that is intended to both support research activities

in solar resource assessment and to assist in performing actual site surveys. The development process of the prototype has attempted to address some of the shortcomings identified in the existing tools by Duluk et al. (Duluk et al., 2013). Besides serving as a proof of concept for site survey tools on Android devices, this tool is intended to provide a platform that will allow other researchers using the tool to intelligently assess its scientific value and to make educated decisions about how it can best be applied to support resource assessment, and to further research on solar site assessment techniques.

2. Description of the Android platform

The Android platform is an open-source operating system that is currently developed by Google, Inc. It is based on the Linux operating system. Android based smartphones were first released in 2008 (Helft and Holson, 2008). Phones being released in 2015 typically run version 5.0, nicknamed "Lollipop," though versions are updated regularly. Software for Android comes in the form of Applications, frequently called "apps," which are primarily developed using the Java programming language (Google, 2015a). Prototype applications have been demonstrated that make use of the phone as an "Augmented Reality" (AR) tool, displaying visual information to the user via the camera display (Tokusho and Feiner, 2009). AR applications utilize similar capabilities to those required to perform a solar site assessment. While the technical capabilities of Android-based smartphones compare to those of a traditional computer (ability to perform computations and access the internet), computational speeds may be somewhat slower due to the variability in available phone processors and hardware. Besides the obvious portability, there are several other features of smartphones that make them an attractive option for solar site survey applications.

Most Android smartphones include a variety of sensors that can be used to acquire data. Some examples of the types of sensors available on the phone include: cameras, accelerometers, gyroscopes, magnetometers, GPS/location sensors, pressure sensors, and light sensors (Google, 2015b). The Android operating system provides an interface to these sensors through the use of a "SensorManager," which allows code to register for updates when new sensor data is available. Several acquisition rates for sensors are available using generic descriptions that correspond to approximate time delays between updates. The delay rates of Game (20ms) and Fastest (0ms) are most appropriate for AR applications that require sensing of the phone orientation. The slower rates are available, such as Normal (200ms), are better suited for detecting gross screen orientation changes, an application where real-time orientation is not important. It should be noted that unlike typical data acquisition, Android uses chosen acquisition rates as "suggested delays" and shorter delays (i.e. faster rates) may be used by the operating system if system resources are available (Google, 2015b). Timestamps provided with sensor updates can be used to determine the actual sampling rate of the data, if required. Data at the "Game" rate would be expected to be appropriate for augmented reality applications, assuming computational resources are adequate to perform calculations at that rate. Practical testing is anticipated to be the best method to determine whether computational resources are sufficient to perform necessary site survey calculations.

While accelerometers and magnetometers constitute the physical hardware used to provide sensor data on Android smartphones, a layer of software exists between the sensors and the programming environment. This allows Android to provide access to several composite sensors that simultaneously make use of data from more than one sensor (Google, 2015c). An example is the

RotationVector sensor accessible within the operating system. This sensor fuses data from accelerometers, gyroscopes and magnetometers to provide an absolute, 3D vector representing the spherical orientation of the phone. An algorithm for performing the sensor fusion is provided with the operating system, and generally represents the best practices for obtaining this data. Functions built into the operating system also allow the coordinate system of this vector to be transformed to suit user-specified axes.

Some preliminary work has investigated the uncertainty of Android sensors for data acquisition purposes (Ayub et al., 2012; D'Elia and Paciello, 2012), but at present, no detailed study of the reliability of phone-made measurements is available. Generally, the azimuth orientation has been observed to the most variable measurement. A study by Blum et al. (Blum et al., 2013), investigated uncertainties in compass heading as a result of walking through an urban environment and found that compass azimuth readings were typically within 10° of expected values, but experienced excursions as high as 30°. This was attributed to the sensitivity of the magnetometer sensor (on which azimuth is based) to local magnetic field variability caused by large metal objects (e.g. structures and cars). While this provides a starting point for interpreting sensor uncertainty, several challenges are faced by any attempt to actually quantify the uncertainty of smartphone sensors in more detail. Examples of challenges are:

- variability in sensor hardware (across manufacturers and models)
- variability in software implementations of the sensor hardware interface
- variability in "point-of-use" in user behavior associated with different application types

As with computational capability, practical demonstration may be the best way to observe the uncertainties associated with an intended use case.

Besides sensor data, Android provides an interface to access geographic location data. The location (latitude, longitude) is available from a LocationManager interface within the Android development environment. The LocationManager is used to obtain location data from (in order of increasing accuracy): 1) cellular towers, 2) wi-fi networks and 3) built-in GPS (Google, 2015d). The Location Manager provides the most accurate and most recent information available automatically, subject to a specified minimum accuracy. Specifying the minimum accuracy carries the caveat that more accurate location readings may take longer to obtain or may even be unavailable depending on the environment. For example, GPS locations provide the highest accuracy, but may be unable to be obtained indoors. The worst case location uncertainty reported in determining the phone's location is around 10km, which can occur when location is obtained from cellular towers. This accuracy is likely to be sufficient to produce solar site survey estimates similar to those provided by commercial tools.

Based on the preceding discussion, the Android platform can be seen to provide the basic capabilities necessary to perform a solar site survey and related calculations. Several questions remain as to the practicality of such an application: What level of uncertainty will be introduced into the horizon measurement? Will this be dominated by user error or sensor error? Are processor speeds sufficient to perform the necessary computations in a timely manner? Can a real-time, augmented reality sun chart display be produced given the computational resources? These questions are difficult to answer on an *a priori* basis due to the number of variables affecting each. Therefore, a prototype application has been developed (and the methodology validated) in order to assess the suitability of the Android platform for performing site survey operations, and to address these concerns via practical demonstration.

3. Prototype Site Survey Tool Development

The tool developed and validated in this study operates on a smartphone platform in order to leverage the built-in sensor and camera hardware available on modern devices. The tool is available as an open source project (Ranalli, 2014) and runs on smartphones that use the Android operating system. Fig. 1 shows a visualization of the data flow within the tool and highlights some of the major inputs and outputs. The primary purpose served in site surveying is to allow users to measure the horizon in a given location. Additionally, the tool provides the capability to estimate the available solar irradiance in a location subject to the measured shading, to estimate the optimum collector orientation based on the shaded irradiance, and to provide some simple graphical visualizations of the irradiance. Testing of the tool was performed on a Motorola Moto X (second generation) smartphone operating on the Android 5.0 operating system.

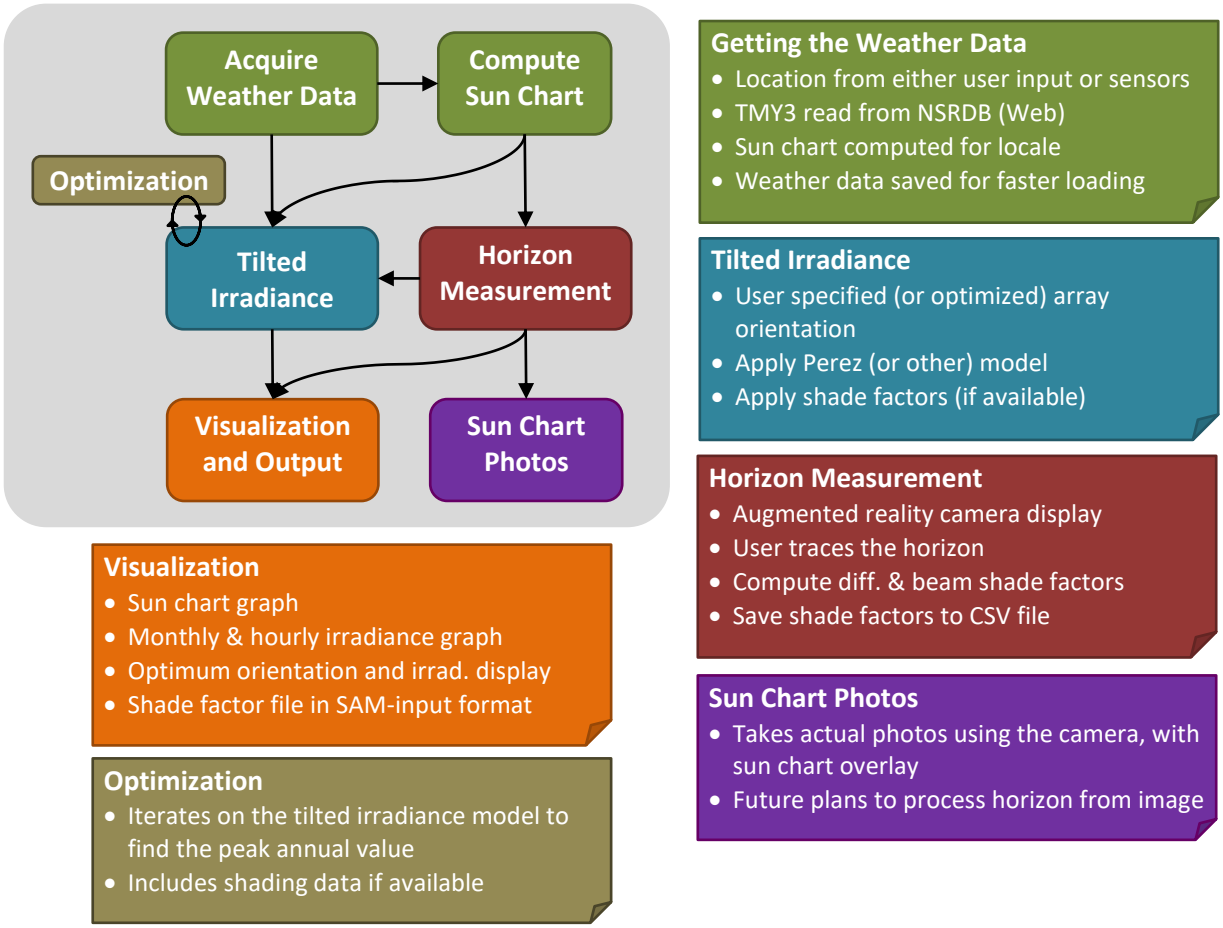

Fig. 1 - Flowchart of program calculations and data paths

Following the data flow in Fig. 1, in order to perform solar irradiance calculations, a geographic location is used to identify a nearby site with available Typical Meteorological Year 3 (TMY3) solar resource data. This resource data is combined with a user specified array orientation to form the inputs to a tilted irradiance model (e.g. Perez, see section 3.6.2). The tilted irradiance model is used to provide

estimates of the annual and monthly irradiance available in the location for the tilted surface specified. Optimization capabilities are used to calculate the optimal tilt and azimuth for the collector using the specified irradiance model. The optimization routine used is a simplex direct-search algorithm, which is available as part of the Apache Commons Math 3.2 library (The Apache Foundation, 2015). Due to the repetitive nature of optimization calculations, optimization is one of the computationally expensive tasks used in the app, and in which processor performance may be limiting. The shaded irradiance optimizations on the test device (2.5 GHz Qualcomm Snapdragon 801 processor) were completed in approximately 6 seconds, which was deemed acceptable for practical use. As such, the computational capabilities of the phone appear to be sufficient to perform the most expensive calculations in a reasonable timeframe.

Measurements of the horizon are made using an augmented reality tool based on the smartphone camera, discussed in more detail in section 3.4. These measurements are processed in combination with the solar position to produce an hour-by-hour list of shade factors. These shade factors are used by the irradiance model and the optimization routine to compute the reduction in irradiance and the adjusted optimum collector orientation. Besides these in-app numerical outputs, visualizations are provided in the form of monthly irradiance graphs (showing shaded and unshaded values), and comma-separated value file outputs. The comma-separated value output files are suitable for use as inputs to System Adviser Model (SAM), a software package developed by the National Renewable Energy Lab (NREL), capable of performing photovoltaic system modelling and economic analysis (Blair et al., 2014).

The following sections provide details on specific behaviors of the tool.

3.1. Resource Data

TMY3 resource files are used to provide estimates of the available irradiance. While TMY3 files are not considered to be “bankable” (Vignola et al., 2012), they are useful in providing an estimate of the long-term performance of a solar system, and can serve as an entry point to more detailed analysis that includes year-to-year variability and extremes in the statistical expectation of the available resource. Users who require the additional level of statistical data could still use the horizon outputs of the application to generate shading estimates that could be used in conjunction with detailed annual resource data and computer-based solar analysis packages. The TMY3 resource files are obtained from the National Solar Radiation Database (Wilcox, 2012) using the smartphone’s internet connection. These files are processed to extract hourly values of Global Horizontal Irradiance, Diffuse Horizontal Irradiance and Direct Normal Irradiance. Since files are directly accessed from the database, data from all TMY3 stations are available. By default, the station with the closest geographic distance to the specified location is chosen, but users may manually choose a different station. One limiting aspect of this data source is that irradiance data can only be computed for United States locations. In principle, additional online solar resource data sets could be integrated in the future based on community involvement or interest. TMY3 files are approximately 1 megabyte (MB) in size, and their download rate depends primarily on the user’s internet connection. The additional computational processing of these files was not observed to produce a significant delay.

3.2. Sensors

Data from several sensors that are integrated into the smartphone are used to detect the geographic location of the phone, and to detect the phone's orientation. Location and orientation of the phone are obtained using the services described in Section 2. The phone orientation is obtained by using a RotationVector sensor (Google, 2015c). As stated, this is a composite sensor that combines information from several types of sensors to produce the most accurate reading of the orientation. The Android operating system uses a custom algorithm to combine this data, and the default implementation is used here without modification. The output of the RotationVector is processed to produce values of roll, pitch and azimuth that describe the phone's orientation relative to the user's perspective, holding the phone vertically. Based on qualitative observations, the values for roll and pitch are able to be measured consistently using these sensors. The azimuth reading, as it depends primarily on the output from the magnetometer sensor, is highly sensitive to magnetic interference (Blum et al., 2013), and may produce skewed azimuthal readings. Further analysis of these errors was performed and will be described in Section 4.2.

The location of the phone is obtained using the most recent data provided by the operating system from any source. Within the solar calculations, the location is used for two purposes: finding the nearest available TMY3 station as discussed previously, and in the calculation of the sun chart, used to determine solar incidence angles and shading. The worst case, 10km location uncertainty would be expected to result in sun position errors of less than 1°, which is assumed to be sufficient for prototype purposes given the accuracy of the sensors. Higher fidelity location readings are available as discussed previously, but come with potential for greater delays in obtaining the reading.

3.3. Camera

The phone camera is used to visualize the sun path overlaid into the real world space of the camera's field of view, referred to as augmented reality (AR). Similar approaches to mapping the sun path onto an image exist in the literature (Cellura et al., 2012; Orioli and Gangi, 2012). Sun path lines were shown for each solstice and for each month in-between. The 21st of each month was chosen as the representative date for each month. The tool uses an angular spacing of 5° for the lines of latitude and longitude on the sky dome, and a temporal spacing of 6 minutes for the sun path lines. This resulted in a total of roughly 3000 points that were spherically projected onto the display.

While the individual projection calculations for these 3000 data points are not computationally challenging, the need to perform them repeatedly as the sensor data is obtained in real-time does present a computational capability question. The AR display was updated at an approximate rate of 50 updates per second ("Game" delay) as sensor data was acquired on the test phone. No noticeable performance issues were observed in the AR display on the test device. The display was observed to update in real-time for several minutes without producing any errors associated with failing to consume the data as it was produced, confirming the adequacy of the computational performance.

The ability to save pictures while using the tool in the AR mode was added as a demonstration of the capability. A total of three JPEG images are saved for each snapshot: a standard digital photo directly from the camera, a set of approximate lines against a black background showing the projection of the sun position throughout the year, and a combination of the photo with the lines directly overlaid onto the image. For each picture capture, metadata is saved, providing the orientation of the phone (roll, pitch, azimuth) and the view angles of the camera. In the future, additional development could

apply computer vision techniques to obtain horizon measurements directly from these images. A sample image combining the camera view with the sun path lines is shown in Fig. 2.

Fig. 2- Sample camera output from the app showing the sun path overlaid on the field of view.

3.4. Horizon Tracing

Measurements of the horizon are also made by using the augmented reality view. A crosshair is placed in the center of the camera's field of view and the user is prompted to "trace" the horizon using the crosshair. As the user does so, a list of azimuth/altitude pairs is generated at every sensor update, based on the instantaneous phone orientation. Because the crosshair is located in the center of the camera's view, no projection calculations are necessary to record the indicated horizon; the azimuth and pitch of the phone correspond directly to the azimuth and altitude of the identified horizon point. This list of points generated is stored, representing the entire visible horizon from the point of view of the camera. The points are used to determine shading as discussed in section 3.6.8.

In addition, output files are generated based on this horizon that can be used by other software packages. The horizon profile is output directly as a series of azimuth and altitude pairs. Other files containing the diffuse shade correction factor based on the specified orientation, and a list of hourly beam shade factors (see section 3.6.7) are generated as well. These files provide the information needed to perform a photovoltaic system analysis using a computer-based software tool, such as SAM. Files may be transferred to a computer using the phone's standard USB interface.

3.5. File Output Structure

Several file outputs are produced by the tool. Measurements are structured as named "projects," for which a directory is created in the smartphone storage space. Several comma-separated value (CSV) file outputs are used to maintain the project state and allow saving/loading of an existing project. These include files that store a subset of the TMY3 file, the list of azimuth/altitude points that represent the horizon and the project settings and configuration (e.g. the specified array orientation). The weather file subset in particular is used to eliminate the need to repeatedly download the TMY3 file every time a project is loaded. In addition, several data files are created that can be used as inputs to other tools, such as SAM, as stated previously. These include a file with a list of beam shading factors, a file with the diffuse shading factor at the specified array tilt and azimuth, and a list of the average irradiance (by component) for each month of the year.

3.6. Calculation Methodology Used by the Prototype

3.6.1. Sun Position

The solar positioning algorithm used was based upon the algorithm described in the System Advisor Model reference document (Gilman, 2014), which is in turn based on a method published by Michalsky (Michalsky, 1988). Since this tool does not make any changes to the cited methodology, readers are referred to the literature for the details. The effective solar time is determined from the local time in the TMY3 file. The mid-hour point is used for hours where the sun is up, while the mid-point of the above-horizon time is used for the hours during which sunrise/sunset occurs. Equations from Michalsky use this solar time and Julian day as inputs, and may be used to determine the sun altitude and azimuth. Atmospheric refraction, which primarily affects the position at low altitudes, is included in the calculations.

3.6.2. Tilted Solar Irradiance Resource Modelling

The irradiance on a tilted array surface (termed the slope irradiance) is calculated following methodologies that are commonly available in textbooks and the literature. These models divide the total slope irradiance (G_t) into three components: the beam, the sky diffuse and the diffuse ground reflected.

$$G_t = G_{bt} + G_{dt} + G_{gt} \quad (1)$$

The primary difference between modelling approaches for these three components occurs in determination of the sky diffuse irradiance. Three such diffuse sky models are implemented in Solar Survey. They are: Isotropic Sky, the model of Perez et al. (Perez et al., 1990) and the model of Muneer et al. (Muneer, 2004). The Isotropic Sky model is the simplest and oldest model, but is generally considered to have been superseded by the more recent anisotropic sky models. The Perez model has been widely used for modeling of the solar irradiance in the United States and is the default model used by SAM. The Muneer model has also been applied for modelling of irradiance in the United States (Lave and Kleissl, 2011), and is implemented here as a supplement to the other models.

Like the solar position algorithms, the implementations of the Isotropic and Perez models follow those discussed in the reference documentation for the System Advisor Model software (Gilman, 2014). The implementation of the Muneer model is based on the approach used by Lave and Kleissl (Lave and Kleissl, 2011), incorporating near-horizon effects as described by Page (Page, 2003). While readers are

referred to the literature for detailed descriptions of these models, an overview is provided here as a supportive reference to the software implementation being discussed.

3.6.3. Terms Common to All Models

The approach for calculating the beam and ground reflected terms are common to all diffuse sky model approaches. For the beam:

$$G_{bt} = G_{bh} \frac{\cos\theta}{\cos\theta_z} \tag{2}$$

The ground reflected component relies upon the ground albedo, the total irradiation on a horizontal surface and the view factor between the tilted surface and the ground.

$$G_{gt} = \frac{1-\cos\beta}{2} \rho (G_{bh} + G_{dh}) \tag{3}$$

The ground albedo is seldom present in the meteorological data files, and an assumed value must be used for months where it is absent. The sporadic nature of its presence can result in some "artificial" month-to-month variation in ground reflected irradiance when comparing months with and without albedo data. As a result, the tool presently assumes that the albedo always takes a constant value of $\rho = 0.2$. As the ground reflected irradiance is typically one or two full orders of magnitude smaller than the other slope irradiance components, the effect of this assumption may be considered to be negligible.

3.6.4. Isotropic Model for Diffuse Sky

The Isotropic model uses the simplest approximation for the diffuse irradiance on a tilted surface. The approximation assumes that the sky is a uniform radiation source, resulting in a computation based on the view factor between the ground and the sky and on the diffuse horizontal irradiance.

$$G_{dt} = G_{dh} \frac{1+\cos\beta}{2} \tag{4}$$

3.6.5. Perez Model for Diffuse Sky

The Perez model breaks the diffuse sky up into three components. They are the isotropic component, the circumsolar component and the horizon brightening component (Gilman, 2014). The total sky diffuse irradiance on a tilted surface is then the sum of the three. Computation of the components is a multi-step process. First, parameters *a* and *b* are computed

$$a = \begin{cases} 0 & \cos\theta < 0 \\ \cos\theta & \text{otherwise} \end{cases} \tag{5}$$

$$b = \begin{cases} \cos 85° & \cos\theta < \cos 85° \\ \cos\theta & \text{otherwise} \end{cases} \tag{6}$$

Clearness is computed as:

$$\varepsilon = \frac{(G_{dh}+G_{bh})/G_{dh}+\kappa\theta_z^3}{1+\kappa\theta_z^3} \tag{7}$$

The value for κ is a constant with value 5.535 x 10^{-6} for angles in degrees. The clearness is used to select values of parameters f11, f12, f13, f21 and f22 from the following table.

Table 1 – Clearness index bins for the Perez diffuse sky model (Gilman, 2014).

ε<	f11	f12	f13	f21	f22	f23
1.065	-0.0083117	0.5877285	-0.0620636	-0.0596012	0.0721249	-0.0220216
1.23	0.1299457	0.6825954	-0.1513752	-0.0189325	0.065965	-0.0288748
1.5	0.3286958	0.4868735	-0.2210958	0.055414	-0.0639588	-0.0260542
1.95	0.5682053	0.1874525	-0.295129	0.1088631	-0.1519229	-0.0139754
2.8	0.873028	-0.3920403	-0.3616149	0.2255647	-0.4620442	0.0012448
4.5	1.1326077	-1.2367284	-0.4118494	0.2877813	-0.8230357	0.0558651
6.2	1.0601591	-1.5999137	-0.3589221	0.2642124	-1.127234	0.1310694
infinity	0.677747	-0.3272588	-0.2504286	0.1561313	-1.3765031	0.2506212

A second clearness index, Δ, is computed using the air mass, AM_0, as follows

$$AM_0 = \frac{1}{\cos\theta + 0.15(93.9° - \theta_z)^{-1.253}} \tag{8}$$

$$\Delta = G_{dh}\frac{AM_0}{1367} \tag{9}$$

The Perez model coefficients can then be calculated.

$$F_1 = f_{11} + \Delta f_{12} + \theta_z f_{13} \tag{10}$$

$$F_2 = f_{21} + \Delta f_{22} + \theta_z f_{23} \tag{11}$$

If the calculation for F_1 produces a negative value, it is coerced to zero. The three components of the diffuse sky irradiance (isotropic, circumsolar and horizon brightening) can then be calculated.

$$G_{d,iso} = G_{dh}(1 - F_1)\frac{1+\cos\beta}{2} \tag{12}$$

$$G_{d,cir} = G_{dh}F_1\frac{a}{b} \tag{13}$$

$$G_{d,hor} = G_{dh}F_2\sin\beta \tag{14}$$

In the special circumstance where the solar altitude is less than 2.5°, only the isotropic component is considered.

$$G_{d,iso} = \frac{1+\cos\beta}{2} \tag{15}$$

$$G_{d,cir} = 0 \tag{16}$$

$$G_{d,hor} = 0 \tag{17}$$

In either case, the sum diffuse sky irradiance is

$$G_{dt} = G_{d,iso} + G_{d,cir} + G_{d,hor} \quad (18)$$

3.6.6. Muneer Model for Diffuse Sky

The sky diffuse irradiance by the Muneer model is a multi-step calculation. The Muneer approach considers a two component isotropic sky, a circumsolar component and sky background component (Muneer, 2004). The methodology used here follows that adopted by Lave and Kleissl (Lave and Kleissl, 2011), which adapts from Page (Page, 2003), but is ultimately based on the original Muneer methodology. First a clearness index, K_b, is computed based on the beam irradiance:

$$K_b = \frac{G_{bh}}{\epsilon 1367 \sin \alpha_s} \quad (19)$$

The term ϵ is the correction for the eccentricity of the earth's orbit according to the formula (Muneer, 2004):

$$\epsilon = 1 + 0.033 \cos\left(360° \frac{n-2}{365}\right) \quad (20)$$

where *n* represents the integer day of the year. This is used to compute the empirical function, *f*, that will be used in the correlation for diffuse irradiance. A correlation proposed for Southern Europe is used as representative of the United States, following the approach of Lave and Kleissl.

$$f = \cos^2\left(\frac{\beta}{2}\right) + \left(0.00263 - 0.7120\, K_b - 0.6883\, K_b^2\right) * \left[\sin\beta - \beta\cos\beta - \pi \sin^2\left(\frac{\beta}{2}\right)\right] \quad (21)$$

The diffuse irradiance can then be computed as the sum of the sky background term and the circumsolar term.

$$G_{dt} = G_{dh}\left[f(1 - K_b) + K_b \frac{\cos\theta}{\cos\theta_z}\right] \quad (22)$$

This value is considered to be valid for all solar altitudes above 5.7°. For solar altitudes below 5.7°, a modified form is used as described by Page (Page, 2003):

$$G_{dt} = G_{dh} \cos^2\left(\frac{\beta}{2}\right)\left[1 + K_b * \sin^3\left(\frac{\beta}{2}\right)\right][1 + K_b * \cos^2\theta * \sin^3(\theta_z)] \quad (23)$$

3.6.7. Shading Methodology

A method is needed to compute the effect of the measured horizon on the solar irradiance. Two separate shading factors may be considered: a beam shading factor (f_b) and a diffuse sky correction factor (f_d). The beam shading factor deals with times at which the sun's disk is blocked by an obstacle, while diffuse sky correction factor accounts for the reduction in diffuse sky view factor induced by the horizon. Both of these factors are used multiplicatively in their respective irradiance calculations, and they may take values between zero and one. The tool in this study provides a method for computation of both shading factors, with some caveats that are discussed throughout this section.

A second important aspect of the shading methodology is how it addresses the finite size of the solar collector. A study by Goss et al. (Goss et al., 2014) provides a method to compute the cell-by-cell spatially resolved shading on a module or array. The site analysis tools in the marketplace generally do

not achieve this level of detail, but rather make measurements of the horizon at a single point. Any spatial character to the measurement is then made using averaging; for example, measurements made at each corner of the array may be linearly averaged together to estimate the losses (Galli and Hoberg, 2009). When computing the shading of objects with a high aspect ratio (tall, thin objects) that are near to the collector, this point measurement is limiting. These tall thin objects are likely to shade a two-dimensional collector in a highly time-dependent fashion (shadow sweeping across the array), despite the fact that the single-point shading strategy used in this tool would only predict a short-duration obstacle. More detailed post-processing may be required to accurately estimate the impact of this type of obstacle on an array. The demonstration tool developed here provides only measurement of the horizon at a single location, but averaging of multiple point measurements in post-processing is possible.

3.6.8. Beam Shading Factors

The beam shading factor, f_b, is used to determine the effect of shading on the beam irradiance. This is the most intuitive form of shading factor, related directly to whether the sun itself is obscured by an obstacle. Processing of the horizon profile into a list of shading factors requires an algorithm that can determine whether each solar point is shaded. While in principle, the hourly solar positions could be linearly interpolated to determine part-hour shading, this tool instead employs a binary shading factor for each whole-hour. The hourly shading values are generated using a point-in-polygon test based on the mid-hour sun position, and using the horizon as the polygon boundary. When the sun position falls within the polygon (i.e. is below the horizon), the entire hour is assumed to be shaded, and is assigned a beam shading factor of zero. The point-in-polygon algorithm is adapted from techniques in the literature (Chamberlain and Duquette, 2007).

Point-in-polygon techniques are favorable in that they allow for irregular, concave polygons and need not rely on a "highest obstacle at this azimuth" definition of the horizon. This permits the sun to be "unshaded" when, for example, near the base of a tree with a narrow trunk but a large canopy. The point-in-polygon method used here is modified to accommodate the fact that the measured horizon profile often completely encircles the southern pole. Thus, the southern pole is assumed to be shaded under all conditions. The northern pole is then tested for shading to determine whether the horizon constitutes a "window" or a 360° horizon. While this could allow collectors under an overhang to be considered, it has the consequence of requiring that typical 360° horizon measurements span at least 180° of angle. All horizon profiles are closed by appending the initial azimuth/altitude pair as a terminating point for the profile.

A flow chart detailing the point-in-polygon algorithm is shown in Fig. 3, but a description follows. Rays from the southern pole are traced up to the point of interest, and intersections between the ray and the horizon profile are counted. Initial intersection testing is performed using the bounding box limits (i.e. highest and lowest altitudes) in the horizon profile to reduce computational time. For points found to be within the altitude bounding box, the position is tested against each consecutive pair of horizon profile vertices (that is, each "line" in the horizon profile). If the azimuth of the test point falls between the end-points of the profile line, the line is interpolated on a latitude-longitude basis (Chamberlain and Duquette, 2007), to produce the horizon altitude at the test point azimuth. Special pre-treatment is necessary for the horizon profile vertices in this operation because of the potential wrapping about the 0°/360° point. After considering all possible lines in the horizon profile, the total

count of intersections is determined and the evenness of the number of intersections can then be used to determine whether the point lies within or without of the polygon, that is, is shaded or unshaded.

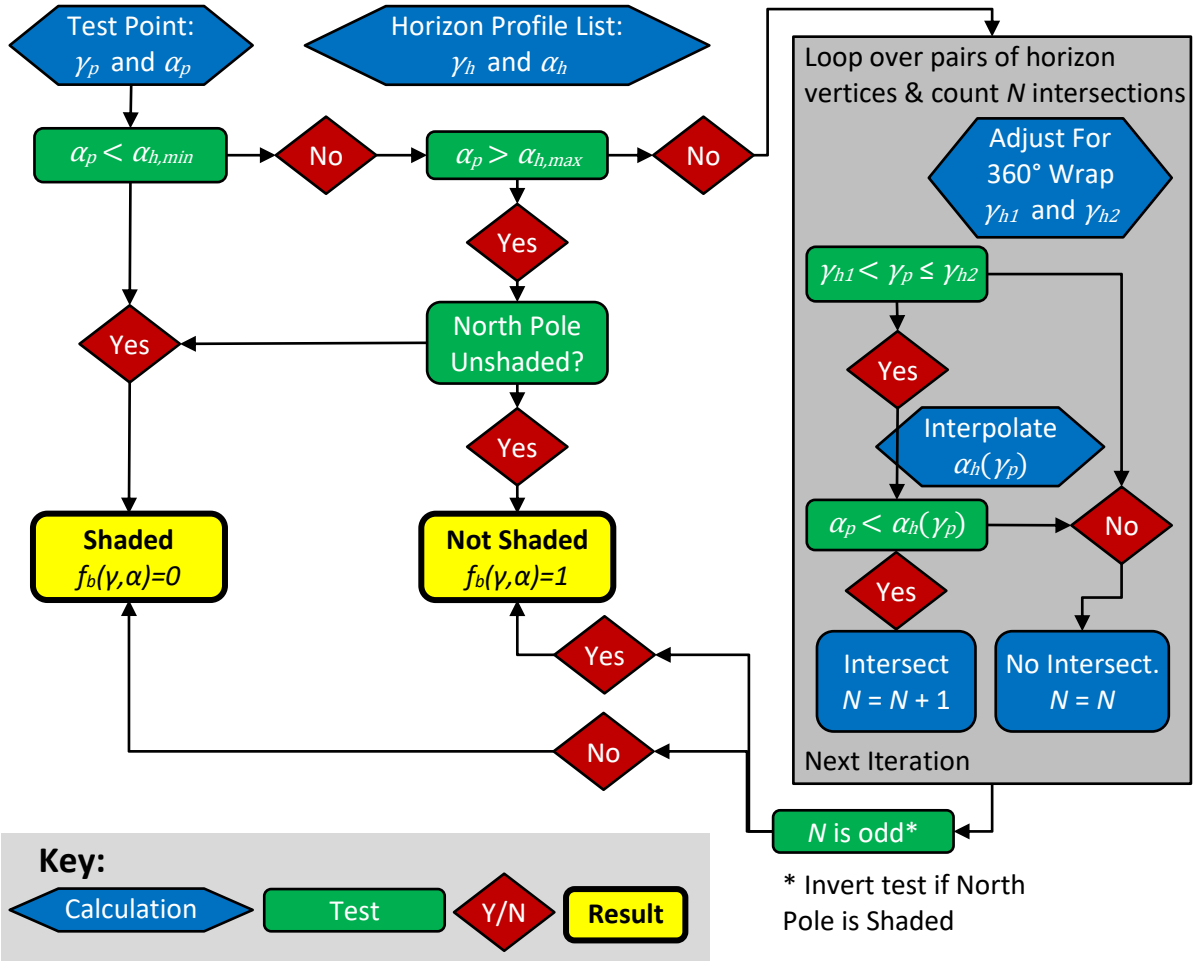

Fig. 3- Flowchart for point-in-polygon algorithm

Two options are available in the tool for the application of the beam shading factor. The option used by SAM assumes that the beam shading factor affects only the beam component of the irradiance, G_{bt}. The beam shading factor is multiplied by the beam irradiance, resulting in zero values of beam irradiance for shaded hours. The second option, proposed by Drif et al. (Drif et al., 2008) for the Perez model, builds upon this. Both the Perez and Muneer anisotropic sky models consider a circumsolar component of the diffuse irradiance that is assumed to originate at the position of the sun. As such, Drif et al. suggest that the circumsolar irradiance should also be affected by the beam shading factor. Both the SAM default and Drif et al. approaches are available in the tool based on user selection, but only the former is able to be validated presently against existing tools (i.e. SAM).

3.6.9. Diffuse Sky Correction Factor

The diffuse sky correction factor accounts for the change in view factor between the collector and the sky due to the presence of the horizon. Since the horizon is empirical, it must be computed by performing the view factor integral numerically. As stated by Quaschning and Hanitsch (Quaschning and Hanitsch, 1995), the form of the view factor integral is:

$$f_d = \frac{\iint S(\gamma,\alpha)\cos\theta\cos\alpha\, d\alpha\, d\gamma}{\pi(1+\cos\beta)/2} \tag{24}$$

The factor $S(\gamma, \alpha)$ represents the shading function, which describes on an azimuth and altitude basis whether the sky is shaded. In this study, the integral is computed numerically by breaking the sky dome up into segments with sizes of $d\alpha = 0.5°$ and $d\gamma = 1°$. This segment size is limited by computational power in the optimization routine. The value of incidence angle, θ, is computed as the great circle angle between a ray pointing to the segment center and the collector normal. The value of $S(\gamma, \alpha)$ is considered based on a binary shading test for each segment (using the same test described for beam shading factors). Cast in this manner, the diffuse sky correction factor essentially considers the diffuse irradiance to be isotropic. The values of $S(\gamma, \alpha)$ are pre-computed and stored when the horizon profile is updated, but the values of θ for each segment must be computed every time the array orientation is altered.

4. Validation and Discussion

4.1. Validation of the Prototype Methodology

The methodologies described were validated using the SAM Simulation Core (SSC) Version 2013-9-20 (National Renewable Energy Lab, 2014). The validation was performed using two metrics, the root mean squared error (RMSE) and the mean bias error (MBE), defined as follows:

$$e = x_{calc} - x_{SSC} \tag{25}$$

$$RMSE = \frac{\sqrt{\sum(e^2)}}{n} \tag{26}$$

$$MBE = \frac{\sum(e)}{n} \tag{27}$$

Validation cases considered only hourly values for which the sun was above the horizon. This was necessary due to the fact that the SSC reports substitute values for all hours where the sun falls below the horizon.

Conditions from five different TMY3 files were used for validation, and are listed in Table 2. Subsequent validation data lists the result for the station with the *highest* RMSE (i.e. worst case error) among the five tests, with the relevant station identified.

Table 2- Validation TMY3 sites

Label	Nearby City	Latitude, Longitude	Station ID#
A	State College, PA	40.72, -77.93	725128
B	Phoenix, AZ	33.45, -111.983	722780
C	San Francisco, CA	37.617, -122.4	724940
D	Miami, FL	25.817, -80.3	722020

E	Chicago, IL	41.983, -87.917	725300

The first validation was performed simply to confirm the accuracy of the sun position algorithm. Incidence angle was calculated assuming a collector at a tilt of 20° and an azimuth 20° west of south. The results are shown in Table 3, and demonstrate the high degree of accuracy in replicating the algorithm.

Table 3 - Validation of Sun Position (Worst case only)

Label	RMSE (deg)	MBE (deg)	Worst Station
Altitude	0.0286	$-6.45*10^{-4}$	A
Azimuth	0.124	-0.00103	A
Inc. Ang.	0.0147	$-3.24*10^{-4}$	A

Validation was then performed to confirm the tilted irradiance models, using the same test collector orientation. As the beam and ground reflected irradiance models are shared between all cases, they were validated together, with one caveat. SSC's implementation of the Isotropic model produces different results for the beam irradiance, due to different conditioning of the data relative to solar zenith limits. As such, the comparisons for beam and ground reflected values were made with the SAM Perez implementation only. As is evident from Table 4, variation for beam and ground reflected irradiance was found to be insignificant.

Table 4 - Beam and Ground Reflected Irradiance Validation (Worst cases only)

Irradiance	RMSE (W/m2)	MBE (W/m2)	Worst Station
Beam	0.00895	$-5.09*10^{-5}$	B
Ground Relfected	0.00745	0.00113	B

The validation of the diffuse irradiance was performed on a model-by-model basis. The isotropic and Perez model outputs were compared to their relevant implementation in SAM. The Muneer model was compared against SAM's Perez implementation for reference, though the comparison is indirect. Table 5 shows that even in the worst case, accuracy was high, with the error around 0.02% of the maximum irradiance for the Perez case. The Muneer case was not expected to have high accuracy due to the fact that it was an indirect comparison, but results still showed a reasonable match. A scatter plot of data is shown for the comparisons for Station B in Fig. 4. Both of the models that are directly implemented closely coincide with the ideal, linear relationship, indicating excellent agreement. Combining the errors associated with beam and ground reflected irradiance, the worst case RMSE for the Perez model total irradiance remained around 0.120 W/m^2.

Table 5 - Diffuse Irradiance Validation (Worst cases only)

Irradiance	RMSE (W/m2)	MBE (W/m2)	Worst

			Station
Isotropic	0.648	-0.536	D
Perez	0.120	$-8.52*10^{-4}$	B
Muneer	9.01	-3.51	B

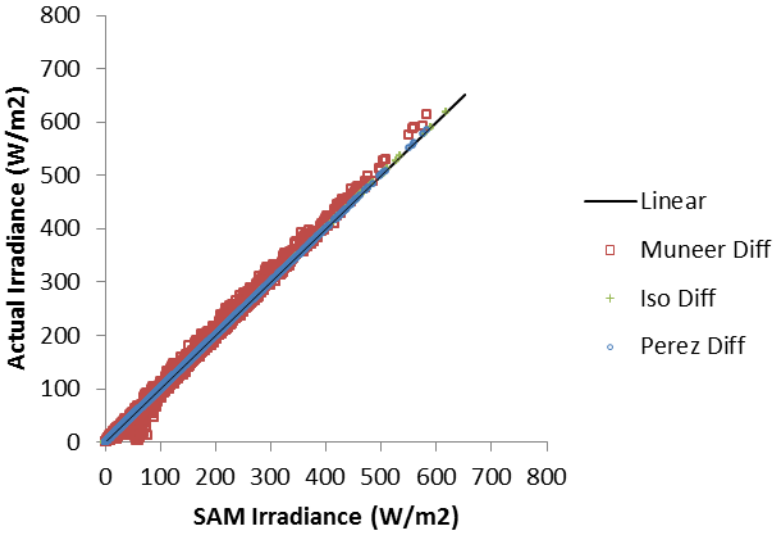

Fig. 4 - Visual comparison of different diffuse models for Phoenix, AZ (Station B)

The shading algorithm was validated on total irradiance, directly against the process used by SAM (i.e. considering the beam shading factors applied only to the beam irradiance). However, as stated in section 3.6.8, an alternate method following Drif et al. (Drif et al., 2008) is available in the tool. The horizon profile used in this validation was an artificially generated, "top-hat" horizon centered at an azimuth of 60° east of south, with a width of 40° in azimuth and a peak altitude of 25°. All azimuths outside this window were assumed to have a horizon altitude of 0°. Fig. 5 shows the effect of this shade profile on a simplified sun chart for reference. The results of the comparison for shaded irradiance at each test station are given for the worst cases in Table 6. As with the unshaded irradiance, the results showed a high correlation between the SAM reference and the tool results. Considering the Perez model, where the most accurate match was desired, the worst case RMSE is 0.118 W/m^2.

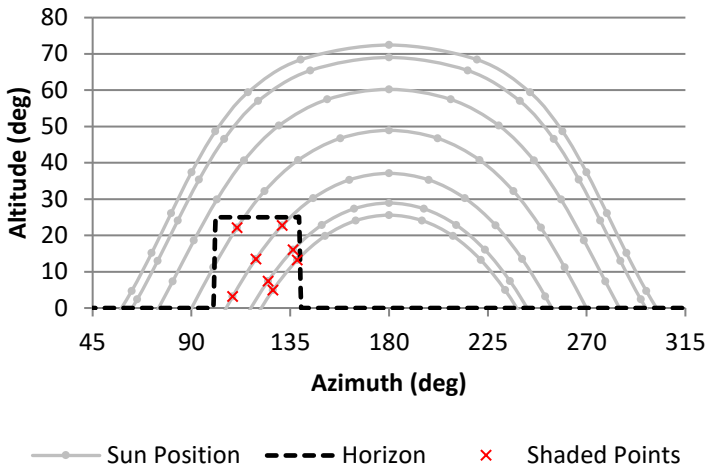

Fig. 5 - Simplified sun chart showing the hours where shading was detected for the flat-top horizon.

Table 6 - Total Irradiance Validation with Shading Included (Worst cases only)

Irradiance	RMSE (W/m2)	MBE (W/m2)	Worst Station
Isotropic	8.54	1.73	B
Perez	0.118	$3.08*10^{-4}$	B
Muneer	8.85	-3.43	B

A final set of validations were performed to compare the optimum orientations computed by the tool. Table 7 lists optimum azimuth and tilt computed for the five weather stations, for each of the models. In addition, validation was performed using the same artificial horizon profile described previously to simulate shading. The optimum orientations computed for each station subject to this shading are shown in Table 8. Two major observations may be made from these data. First, the maximum deviation between the tool implementation of the Perez model and that of SSC was observed to be 0.2 degrees. Second, the shifts observed in the optimum orientation from the unshaded to the shaded condition are consistent with expectations based upon the artificial eastern-sky horizon profile used; i.e. the optimum azimuth shifts to the west while the tilt is reduced.

Table 7 - Optimum orientation for unshaded irradiance, relative to 0° azimuth at due south.

	Isotropic		Perez		Muneer		SSC Perez	
Station	Azi (deg)	Tilt (deg)	Azi (deg)	Tilt (deg)	Azi (deg)	Tilt (deg)	Azi (deg)	Tilt (deg)
A	-0.5	30.3	-1.1	34.7	-1.5	35.1	-1.3	34.7
B	-1.6	28.3	-2.3	31.8	-1.5	31.9	-2.3	31.7
C	6.5	27.6	6.2	32.4	6.4	32.4	6.2	32.5
D	-5.4	20.4	-5.2	24.9	-5.3	25.0	-5.1	24.9
E	-3.3	29.0	-1.4	33.9	-1.8	33.9	-1.4	34.0

Table 8 - Optimum orientation for shaded irradiance, relative to 0° azimuth at due south.

	Isotropic		Perez		Muneer		SSC Perez	
Station	Azi (deg)	Tilt (deg)	Azi (deg)	Tilt (deg)	Azi (deg)	Tilt (deg)	Azi (deg)	Tilt (deg)
A	15.5	28.9	15.3	33.8	13.9	33.7	15.2	33.7
B	14.9	27.1	14.6	30.6	14.0	30.7	14.6	30.7
C	19.3	27.0	19.2	32.4	19.1	32.1	19.3	32.4
D	13.0	18.5	11.8	23.5	11.6	23.3	11.9	23.5
E	12.6	27.1	10.7	32.2	10.5	31.9	10.8	32.2

4.2. Prototype Horizon Measurement Accuracy

The preceding validation shows that the prototype application reliably implemented existing solar calculation methodologies. The chief remaining question is that of the accuracy of the horizon measurement itself, as it acts as an input to the subsequent calculations. Qualitatively, it was observed that the pitch measurement appears to be more reliable than the azimuth. This has been described primarily as a limitation of the type of measurement being made by the smartphone sensor (Blum et al., 2013); the magnetometer is particularly sensitive to the magnetic field of nearby metal objects. In order to investigate how accurately the horizon is able to be measured, quantitative testing has been performed to determine the repeatability and uncertainty associated with this technique.

First, the phone was mounted to a manually controlled, motorized station that was able to be adjusted in both azimuth and altitude. This mount provided a measurement of shift in azimuth and altitude, but lacked absolute readings of these angles. Initial values for azimuth and altitude were therefore referenced to the readings from the phone at the starting data point. This test could thus best be described as a representation of the ability of the Android sensors to accurately reproduce known orientation variations in horizon measurement, which could also be interpreted as drift in the angular readings of the sensors.

Beginning with the phone oriented approximately northward, simulated horizons were measured as the azimuth was varied in either a clockwise (eastward) or counterclockwise (westward) direction for approximately a full circle (365°). Specific altitude levels were chosen for azimuth bands of roughly 45°, resulting in a stair-step horizon pattern. The results are shown in Fig. 6. Differences between the two “known” curves, shown as dashed lines, result from imperfections in the manual control of the motorized mount. Several conclusions can be drawn from this data. First, the accuracy of the altitude is confirmed to be better than that of the azimuth. The maximum deviation from expected value in altitude was approximately 0.5°. The worst case azimuth reading errors were much higher, about 12° from expected. Azimuthal readings were observed to fall both to the east and west sides of the expected value. Despite this error in the accuracy, the precision of the azimuth was observed to be relatively good. Vertical paths on the horizon (where the altitude was varied with constant azimuth), the measured lines remain close to vertical. The error results from the offset of this line from its expected value.

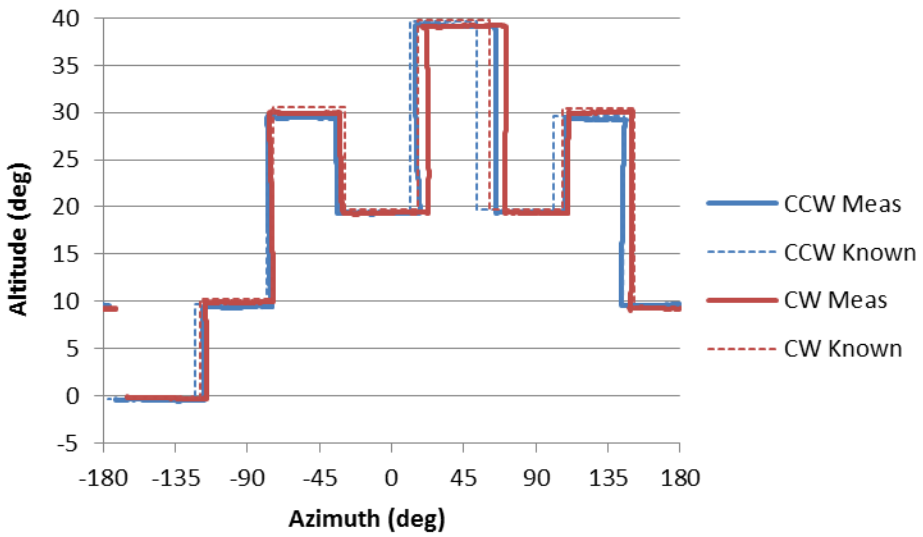

Fig. 6 - Comparison of clockwise (CW) and counterclockwise (CCW) horizon measurement with known positions.

A second validation was conducted to determine the "practical use" repeatability of horizon measurements. A repeated measurement of a sample horizon was made by a user, using the app as intended. Though this repeat measurement provides a sense of the actual use repeatability of the measurement, it cannot be referenced to a "known" value. A panoramic photograph of the sample horizon used for this measurement is shown in Fig. 7. Four clockwise and four counterclockwise measurements were made, with the starting point toward the north, around the left/right edge of the photo. The eight repeated measurements of the horizon are each plotted in Fig. 8. Note that because the horizon was at times double-valued in altitude, only the highest value at each ~1° azimuth bin was used in calculating the mean and other statistics.

Qualitatively, the major features are captured in a relatively repeatable fashion, but fine details show some degree of variation. It is possible to calculate the standard deviation of the altitudes of the horizon traces relative to the mean. The value of this standard deviation is 5.5°. Due to the fact that on a point-by-point basis, the azimuth is more likely to be highly variable, it may be sensible to compare the standard deviation relative to the mean from the perspective of azimuth. This was computed by identifying the shortest distance between the mean horizon profile at a fixed altitude, for each azimuth in the profile. The resultant standard deviation from that calculation was 2.5°. While each of these measures represents the overall "practical use" standard deviation of the eight repeated horizon measurements, some caution should be used in interpretation, as will be discussed in the subsequent paragraph.

As stated, the character of the error in the measurements can be said to not be uncertainty in the form of noise, but rather relatively high azimuth precision with reduced accuracy. That is, the rough shape of each "object" that makes up the horizon is reasonably well maintained. The error manifests as azimuthal shifts of these "objects." It may be more instructive therefore to consider the ability of the measurement to reproduce a specific object on the horizon. The single feature that was observed to have the highest variability is the large tree in the right of the figure. The standard deviation of the

altitude of the tree's peak was around 0.5°, a comparatively high accuracy. On the other hand, the standard deviation of tree's peak azimuth for the 8 cases was 5°. The peak of the tree was measured to occur between 88° and 108° in azimuth throughout the eight repeated measurements. This worst case azimuth error band of 20° is similar to that seen by Blum et al. (Blum et al., 2013). The approximately vertical edges of the tree had a similar limiting variability of roughly 20°. These numbers represent the repeatability with which the same fixed point in space (i.e. object on the horizon) can be measured including both uncertainties in the device capabilities and those associated with practical use.

The impact that this degree of azimuth errors have on the estimates of the solar resource depend on a number of factors. They include:

- the location of the object relative to the sun's position
- the size and shape of the object
- the amount of shift that occurs

Ranalli and Brownson (Ranalli and Brownson, 2014) previously conducted a preliminary investigation on the impact of azimuthal uncertainty on predictions of the solar resource. Their results showed that even large (~40°) errors in the azimuth measurement of a simulated horizon obstacle produced less than 5% impact on the predicted annual irradiance of a collector. The impact of horizon error on the optimum collector orientation was also estimated to be small. This suggests that even the worst case errors observed using the Android platform (20° in azimuth) would not be expected to have a substantial impact on predictions of the irradiance or on guiding orientation of the collector. However, continued study on the relationship between shading uncertainty and predicted irradiance is still warranted.

Fig. 7 - Panoramic photo of the hotizon tested for measurement repeatability.

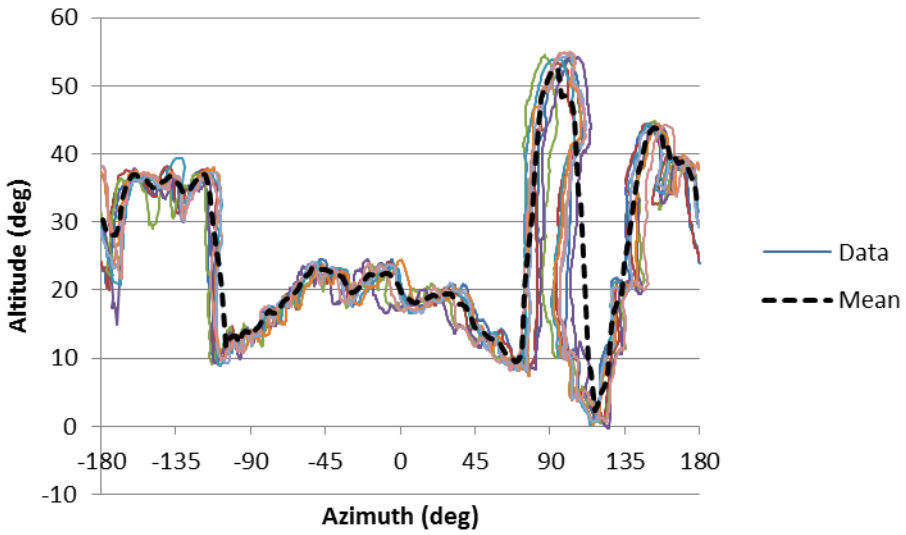

Fig. 8 - Repeated measurements of the horizon shown in Fig. 7.

5. Conclusions

This paper addresses the ability of Android smartphones to serve as a platform for making solar site survey applications and culminates in development of a prototype, open-source solar site survey tool. While the analyses implemented are found in the literature, this tool represents a novel investigation of the Android platform for solar applications, bringing analysis capabilities to a ubiquitous consumer device. The capabilities of Android smartphones were demonstrated to be suited to performing solar site analysis, coming pre-equipped with the sensor technology necessary and the ability to perform the relevant computations. At present the tool serves the need of providing irradiance estimates for a potential solar installation, and allowing measurement of the local horizon, which can serve as an input to computer-based tools such as System Advisor Model (SAM).

As discussed, the tool was able to perform adequately within the constraints of the computational capabilities of the smartphone. The most computationally expensive calculation, optimization of the shaded irradiance, was performed within approximately 6 seconds on the test device. Augmented reality display of the sun chart was able to perform without noticeable lag with a sensor acquisition delay of approximately 20 milliseconds. The sensors used (location and orientation) produced data that served as inputs to the subsequent site analysis calculations. The phone's internet connection was used to access TMY3 data files. Data outputs were accessible via USB connection for input to other computer-based analysis packages. This demonstrates the suitability of current smartphone technology as a computer platform for these types of preliminary solar resource analyses.

The repeatability and uncertainty of the horizon measurement were tested with respect to controlled and "practical use" measurement repetitions. The altitude of obstructions was measurable with a high degree of accuracy, with standard deviations observed around 0.5°. The azimuth showed a reduced accuracy, identifying the location of obstacles only within 20°. Variations in azimuth were observed to occur as shifts of objects in the horizon, maintaining a relatively high precision despite accuracy errors. That is, the overall shape of obstacles was approximately maintained, but their central

azimuth was found to be shifted from the actual. As such, the errors observed are believed to be an artifact of the ability of the sensor itself to obtain an accurate absolute orientation rather than measurement noise. Though preliminary work in the literature suggests that the impact of these errors on solar resource calculations would be relatively small, further study targeted specifically at the impact relative to this type of horizon measurement is warranted.

The validation performed in this paper provides documentation of the prototype tool's performance relative to established tools in the field and is a stepping-stone for further research in the area of tool-assisted solar site analysis. The validation showed that the implementation of the models agreed very well with SAM, which was used as a reference for similar solar irradiance calculations. The implementation of the Perez model in the tool matched the SAM implementation of the same to an accuracy of better than 0.1% of the maximum irradiance. Validations of the optimization also performed consistently between the tool and SAM. At this point, this tool can be used with confidence that the same results as SAM can be achieved for the same models.

Several areas of future work are ongoing as development and research in this area. Due to accuracy concerns related to the smartphone azimuth measurement, additional research is planned to identify the effect of errors in the horizon azimuth on the overall shaded irradiance computations. Additionally, while measurements of the horizon made using the horizon tracing approach in this tool are adequate, the convenience of photographic horizon measurements would enhance the overall usability. It is also possible that this may assist in correcting some of the azimuthal uncertainty, due to the ability to match edges of the photographs in a panoramic fashion. Additional work on developing computer vision approaches to identify the horizon from images is planned for the future. It is hoped that Solar Survey will both serve as a demonstration of the Android smartphone as a viable platform for site survey applications, and as a stepping stone for future research on site survey and horizon measurement methodologies.

Acknowledgements

The author would like to acknowledge several important contributors to and supporters of this work. Penn State Hazleton provided financial support through a Butler Research Development Grant. Dr. David Starling assisted with acquisition of the horizon uncertainty data and provided comments on draft manuscripts. Programming assistance on the application was provided by undergraduate students Matthew Caccese and Kurt Schaarschmidt, as well as Jesse Fox and Niraj Pathak of Innovatrix Labs, LLC.

Symbols

f_x – shading factor (beam or diffuse)
G – irradiance (see subscripts below)
θ – angle of incidence between sun and collector surface normal
θ_z – solar zenith angle
α_s – solar altitude angle
γ_s – solar azimuth angle
γ_c – collector azimuth angle
α_h – solar altitude angle of a point in the horizon list
γ_h – solar altitude azimuth of a point in the horizon list

β – collector tilt angle
ρ – ground albedo
e – error
n – number of elements

Subscripts
x – lack of subscript on an irradiance value represents total irradiance

x_b – beam component
x_d – diffuse component
x_g – ground reflected component
x_t – irradiance on tilted surface
x_h – irradiance on horizontal surface
x_n – irradiance normal to the sun's rays
x_{calc} – value produced by the developed tool
x_{SSC} – value produced by the SAM Simulation Core (SSC)

6. References

Ayub, S., Bahraminisaab, A., Bahram, H., 2012. A Sensor Fusion Method for Smart phone Orientation Estimation. Presented at the 13th Annual Post Graduate Symposium on the Convergence of Telecommunications, Networking and Broadcasting, Liverpool.

Bishop, J.W., 1988. Computer simulation of the effects of electrical mismatches in photovoltaic cell interconnection circuits. Sol. Cells 25, 73–89. doi:10.1016/0379-6787(88)90059-2

Blair, N., Dobos, A.P., Freeman, J., Neises, T., Wagner, M., Ferguson, T., Gilman, P., Janzou, S., 2014. System Advisor Model, SAM 2014.1.14: General Description. National Renewable Energy Laboratory.

Blum, J.R., Greencorn, D.G., Cooperstock, J.R., 2013. Smartphone Sensor Reliability for Augmented Reality Applications, in: Zheng, K., Li, M., Jiang, H. (Eds.), Mobile and Ubiquitous Systems: Computing, Networking, and Services, Lecture Notes of the Institute for Computer Sciences, Social Informatics and Telecommunications Engineering. Springer Berlin Heidelberg, pp. 127–138.

Cellura, M., Di Gangi, A., Orioli, A., 2012. A photographic method to estimate the shading effect of obstructions. Sol. Energy 86, 886–902. doi:10.1016/j.solener.2011.12.018

Chamberlain, R.G., Duquette, W.H., 2007. Some algorithms for polygons on a sphere. JPL Publ., 07-03. doi:http://hdl.handle.net/2014/40409

D'Elia, M.G., Paciello, V., 2012. Sensors Uncertainty on an Android Smart Phone. Presented at the Instrumentation and Measurement Technology Conference (I2MTC), 2012 IEEE International, IEEE, Graz, Austria, pp. 698–702. doi:10.1109/I2MTC.2012.6229460

Drif, M., Pérez, P.J., Aguilera, J., Aguilar, J.D., 2008. A new estimation method of irradiance on a partially shaded PV generator in grid-connected photovoltaic systems. Renew. Energy 33, 2048–2056. doi:10.1016/j.renene.2007.12.010

Duluk, S., Nelson, H., Kwok, A., 2013. Comparison of Solar Evaluation Tools: From Learning to Practice, in: Proceedings of the 42nd ASES Annual Conference. Presented at the Solar 2013, American Solar Energy Society, Baltimore, MD.

Galli, M., Hoberg, P., 2009. Solar Site Evaluation Tools & Techniques to Quantify & Optimize Production. Sol. Pro.

Gilman, P., 2014. SAM Photovoltaic Model Technical Reference [WWW Document]. URL https://sam.nrel.gov/reference (accessed 10.14.14).
Google, 2015a. Android Developers [WWW Document]. URL http://developer.android.com/develop/index.html (accessed 1.21.15).
Google, 2015b. Sensors Overview | Android Developers [WWW Document]. URL https://developer.android.com/guide/topics/sensors/sensors_overview.html (accessed 5.23.15).
Google, 2015c. Motion Sensors | Android Developers [WWW Document]. URL https://developer.android.com/guide/topics/sensors/sensors_motion.html (accessed 1.22.15).
Google, 2015d. Location Strategies | Android Developers [WWW Document]. URL https://developer.android.com/guide/topics/location/strategies.html (accessed 1.22.15).
Goss, B., Cole, I., Betts, T., Gottschalg, R., 2014. Irradiance modelling for individual cells of shaded solar photovoltaic arrays. Sol. Energy 110, 410–419. doi:10.1016/j.solener.2014.09.037
Helft, M., Holson, L.M., 2008. With Google Phone, HTC Comes Out of the Shadows. N. Y. Times.
Lave, M., Kleissl, J., 2011. Optimum fixed orientations and benefits of tracking for capturing solar radiation in the continental United States. Renew. Energy 36, 1145–1152. doi:10.1016/j.renene.2010.07.032
Michalsky, J.J., 1988. The Astronomical Almanac's algorithm for approximate solar position (1950–2050). Sol. Energy 40, 227–235. doi:10.1016/0038-092X(88)90045-X
Muneer, T., 2004. Solar Radiation and Daylight Models, 2 edition. ed. Routledge, Oxford ; Burlington, MA.
National Renewable Energy Lab, 2014. SAM Simulation Core SDK | System Advisor Model (SAM) [WWW Document]. URL https://sam.nrel.gov/content/sam-simulation-core-sdk (accessed 12.23.14).
Orioli, A., Gangi, A.D., 2012. An improved photographic method to estimate the shading effect of obstructions. Sol. Energy 86, 3470–3488. doi:10.1016/j.solener.2012.07.027
Page, J., 2003. 1 - The Role of Solar Radiation Climatology in the Design of Photovoltaic Systems, in: Markvart, T., Castañer, L. (Eds.), Practical Handbook of Photovoltaics. Elsevier Science, Amsterdam, pp. 5–66.
Perez, R., Ineichen, P., Seals, R., Michalsky, J., Stewart, R., 1990. Modeling daylight availability and irradiance components from direct and global irradiance. Sol. Energy 44, 271–289. doi:10.1016/0038-092X(90)90055-H
Quaschning, V., Hanitsch, R., 1995. Shade Calculations in Photovoltaic Systems. Presented at the ISES Solar World Conference, Zimbabwe.
Ranalli, J., 2014. Solar Survey — Bitbucket [WWW Document]. URL https://bitbucket.org/jar339/solar-survey (accessed 2.17.15).
Ranalli, J., Brownson, J.R.S., 2014. Sensitivity of Shading Calculations to Horizon Measurement Accuracy, in: Proceedings of the 43nd ASES Annual Conference. Presented at the Solar 2014, American Solar Energy Society, San Francisco, CA.
Smith, A., 2015. U.S. Smartphone Use in 2015. Pew Res. Cent. Internet Am. Life Proj.
Solar Pathfinder, 2008. Instruction Manual for the Solar Pathfinder [WWW Document]. URL http://www.solarpathfinder.com/pdf/pathfinder-manual.pdf (accessed 2.17.15).
Solmetric Corporation, 2011. Solmetric SunEye 210 Series Users Guide [WWW Document]. URL http://resources.solmetric.com/get/Solmetric%20SunEye%20200%20Series%20Users%20Guide_en.pdf (accessed 2.17.15).
The Apache Foundation, 2015. Apache Commons Math [WWW Document]. URL http://commons.apache.org/proper/commons-math/ (accessed 2.5.15).
Tokusho, Y., Feiner, S., 2009. Prototyping an Outdoor Mobile Augmented Reality Street View Application, in: In Int'l Symp. Mixed and Augmented Reality (ISMAR.

Vignola, F., Grover, C., Lemon, N., McMahan, A., 2012. Building a bankable solar radiation dataset. Sol. Energy, Progress in Solar Energy 3 86, 2218–2229. doi:10.1016/j.solener.2012.05.013
Wilcox, S., 2012. National Solar Radiation Database 1991-2010 Update: User's Manual (No. NREL/TP-5500-54824). National Renewable Energy Laboratory.